# Design of De-tumbling Device for Improving the De-tumbling Performance of Uncooperative Space Target

Lei Du[1,2], Zhen Chen[1,2], Hengzai Hu[1,2*], Xiangdong Liu[1,2,3], and Youguang Guo[4]

[1]School of Automation, Beijing Institute of Technology, Beijing, China.

[2]Key Laboratory of Drive and Control of Servo Motion System, Ministry of Industry and Information Technology, Beijing, China.

[3]Key Laboratory of Complex System Intelligent Control and Decision, Beijing, China.

[4]School of Electrical and Data Engineering, University of Technology Sydney, Sydney, Australia.

[*]Address correspondence to: hengzai.hu@bit.edu.cn



**Abstract**

This article presents the design of an optimal coil structure for two de-tumbling devices, each is carried by a de-tumbling robot. The design is based on electromagnetic eddy currents method and aims to reduce the angular velocity of uncooperative space targets. It proposes an optimization framework with the advantages of safety, and high performance. The magnetic field analytical model is established by the designed coil's structure parameters, and the optimal structure parameters of the coil are determined. To further ensure the maximum magnetic field at the target, the electromagnetic characteristics under different current directions in the two coils are analyzed based on magnetic field analytical model, and their accuracy is verified using finite element method (FEM). Additionally, an improved Maxwell's stress tensor method is proposed to calculate the de-tumbling torque, and its accuracy is assessed using traditional Maxwell's stress tensor and virtual displacement method. The proposed optimal coil structure and its optimization framework can de-tumble over one million targets of various sizes, demonstrating significant universality.

## 1 Introduction

Since the first launch of a man-made satellite in 1957 [1], only 48.9% of satellites have remained operational. However, because of break-ups, explosions, collisions, or anomalous events, the other satellites have lost control. Specifically, according to statistical models orbit provided by ESA's Space Debris Office at ESOC in Darmstadt, Germany, there are over 36500 pieces of space debris of larger than 10 cm in orbit. The number is even more staggering for debris in the 1-10 cm size range, totaling approximately one million. Any of those debris can pose a threat to operational satellites [2]. Our satellite-based infrastructure is essential for a multitude of services on which all of us rely in our daily lives, from communications, meteorological monitoring, space exploration, earth observation and other fields [3]. Therefore, Active Debris Removal (ADR) is conducted to solve the above problems for stabilizing the space debris environment.

Unfortunately, the angular velocity of space debris exceeds the maximum angular velocity of 4~5 deg/s that can be directly captured by a robotic arm. Therefore, to stabilize the debris environment, the first task is to reduce the initial angular velocity of the debris by applying an external torque (i.e., de-tumbling torque). According to generating ways of the external de-tumbling torque, ADR methods are mainly divided into two categories: contact and contactless [4]. Contact-based methods, such as robotic arm [5], tentacle capturing [6, 7], the harpoon and tether-gripper mechanism [8, 9], can provide larger de-tumbling torque. However, they also pose collision risks between the de-tumbling device and the uncooperative space target, leading to the generation of new space debris, which is undesirable when dealing with de-tumbling problem.

To ensure the safety of the de-tumbling tasks, many contactless methods have been studied [10-24]. Among them, the contactless method based on electromagnetic eddy currents method [10-20] has received increasing attention due to the advantages of pollution-free and high safety performance. Compared to contact-based methods, electromagnetic eddy current methods not only effectively avoid the need for complex approach and docking operations but also exhibit a higher tolerance for relative distance and attitude. In comparison to other contactless methods like electrostatic force [21], gas impact [22], and high-energy laser ablation [23], the electromagnetic eddy current contactless method does not cause damage to its integrity. As a result, it has attracted significant attention from scholars in recent years.

Given that the majority of uncooperative space targets are composed of non-magnetic but conductive materials, such as aluminum alloy, this creates a favorable physical condition for employing the contactless method. De-tumbling method based on electromagnetic eddy currents was firstly introduced in 1995 [24]. However, due to the limited external de-tumbling torque, a series of methods were subsequently proposed to enhance the de-tumbling performance. Linear de-tumbling device composed of slots and coils was proposed by [10-11], and its performance was evaluated through fundamental experiments to assess the effectiveness of the de-tumbling system. Later, the authors of this study transformed the linear device into an arc-linear structure [12], which effectively reduces magnetic field dissipation, leading to an enhanced de-tumbling performance. Additionally, single or multiple actively rotating permanent magnets carried by de-tumbling robot was proposed [13-15]. The performance can be also effectively enhanced by increasing the relative velocity between the de-tumbling robot and the target. However, it is worth noting that these methods come with risks of mechanical damage and potential loss of control due to the relatively small de-tumbling distances and complex mechanical structures.

To guarantee the safety of the de-tumbling tasks, a series of methods [16-20] have been proposed to reduce the angular velocity of the target at a larger distance. High temperature superconducting (HTS) coils carried by de-tumbling robot were studied by [16-18], which can enhance the magnetic field to improve the de-tumbling

performance. Next, HTS coils were also applied to electromagnetic formation of two de-tumbling robots [18], which can prevent the net force impact [25] when compared to de-tumbling robot equipped with a single HTS coil [16-17]. Furthermore, HTS technology was applied to multiple coils [19-20], as it generates a higher magnetic field. However, although the above-mentioned methods can improve the de-tumbling performance to some degree, considering the manufacturing cost, magnetic field tolerance, cooling conditions, and material toughness of HTS materials, they may increase the complexity and reliability of the de-tumbling tasks.

Focusing on the uncooperative space target, an optimization framework based on electromagnetic eddy currents method for reducing the angular velocity of the target is proposed. Given that the essential requirements of de-tumbling safety, and high performance, it is necessary to position the coils composed of copper carried by two de-tumbling robots at a safe distance from the target to simultaneously generate a large magnetic field to improve braking performance. To find maximum magnetic field, the geometric structure of the coils is optimized, and the optimal structure parameters of the coils for different distances between coils and target are found, combined with the constraint. In addition, to find the maximum magnetic field, the following works are also investigated, which include 1) designing the coil structure; 2) modeling the magnetic field analytical model based on the designed coil's structure parameters; 3) determining the optimal structure parameters considering the constriction of maximum coil size of the fairing of the launcher; 4) analyzing the electromagnetic characteristics with different current directions in the two coils based on magnetic field analytical model and verified by FEM; 5) proposing an improved Maxwell's stress tensor method for calculating the de-tumbling torque generated by the designed coils, with its accuracy assessed using traditional Maxwell's stress tensor method and virtual displacement method; and 6) computing the de-tumbling torque for various target sizes. Fig. 1 shows the schematic diagram of the de-tumbling system, which mainly consists of the de-tumbling robots, de-tumbling devices composed of an ironless stator and coils, and the uncooperative space target. The unsafe areas and orbits of the de-tumbling devices at farther distances are further shown in Fig. 1, respectively.

The remainder of this paper is as follows. Firstly, the specific flow of the optimization framework is introduced. The mechanism of electromagnetic eddy currents de-tumbling method is analyzed, and the analytical model of the magnetic field is established in “Initial Design and Theory Basis” Section. To ensure the maximum magnetic field at the target, an optimization process is conducted in “Optimization Process” Section, and the accuracy of the established magnetic field model is verified using FEM. This process includes analyzing the optimal structure parameters of the coil for different distances between the target and the coils, and the influence of current direction on the magnetic field. In “Analysis of Optimization Results” Section, the proposed improved Maxwell's stress tensor method is applied to calculate the de-tumbling torque on the target through FEM, based on the optimal model obtained above. Finally, conclusions are provided in “Results and conclusion” Section. The main contributions in this paper can be summarized as follows:

1) To guarantee the highest de-tumbling performance, an optimization framework is proposed, and the optimal structure parameters of the coils are found based on magnetic field analytical model.

2) To obtain the electromagnetic performance of the optimal structure parameters, an improved Maxwell's stress tensor method is proposed to calculate the de-tumbling torque, and thence the accurate value of the de-tumbling torque can be provided for actual de-tumbling tasks.

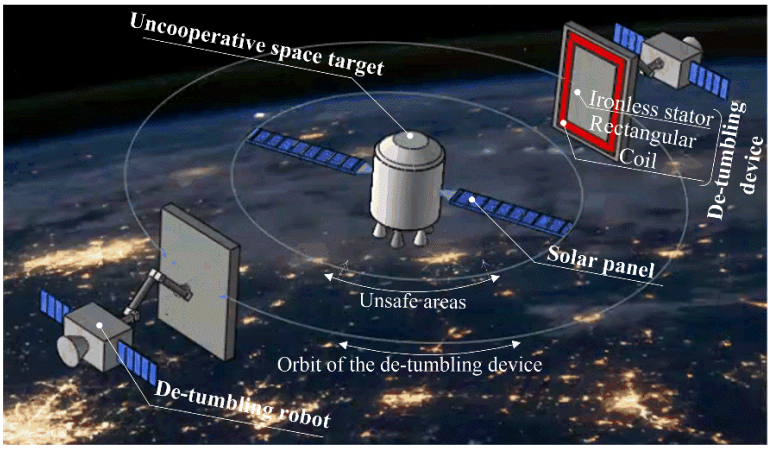


Fig. 1. Schematic diagram of the de-tumbling system.

# 2. Material and Methods

## 2.1 Initial Design and Theory Basis

### 2.1.1 *Design process*

The proposed de-tumbling robot, equipped with coils, is designed for the uncooperative space targets that have a relatively high rotational speed and are not suitable for direct capture by a robot arm. To improve the de-tumbling performance, a comprehensive framework is constructed to guide the optimization of the de-tumbling robot, ensuring that the magnetic field acting on the target is maximum. The specific flow of the proposed optimization scheme is shown in Fig. 2, which can improve the de-tumbling performance and safety.

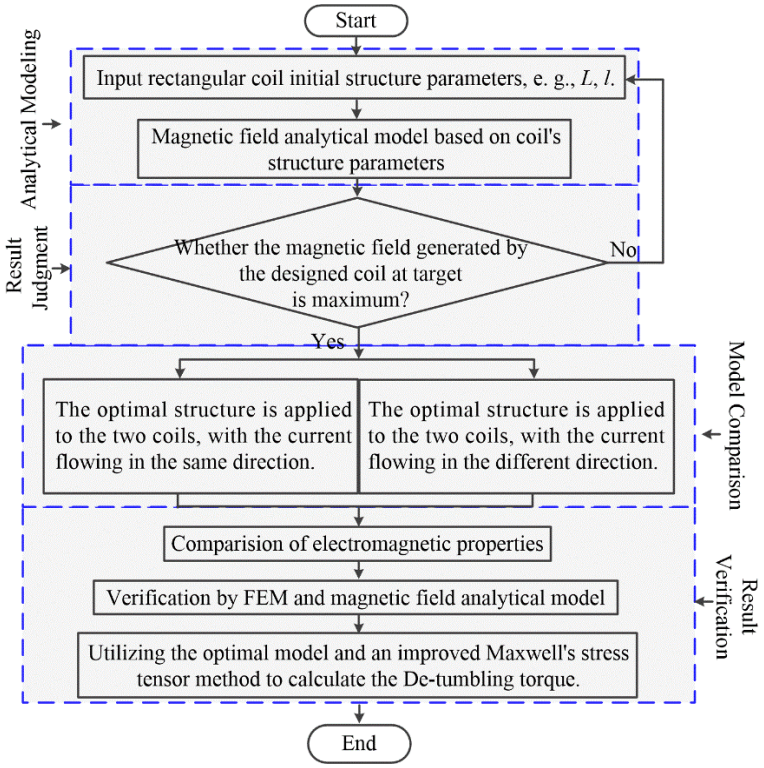


Fig. 2. Specific flow of the optimization scheme.

It is quite difficult to conduct experiments duo to the practical space environment. Thus, some appropriate validation methods are conducted to verify the accuracy of the proposed method. Firstly, optimal structure parameters of the coils at different distances between the target and coils are found based on magnetic field analytical model. Then, the above accuracy is validated using FEM. To obtain the electromagnetic performance of the optimal structure parameters, de-tumbling torque is calculated by the improved Maxwell's stress tensor method and compared with the traditional Maxwell's stress tensor. The accuracy of the proposed method is further verified using virtual displacement method.

### 2.1.2 *Mechanism Analysis of De-tumbling Torque and Structure Design of Rectangular Coil*

To accomplish the de-tumbling task, the interaction between the magnetic flux density $\boldsymbol{B}$ generated by an energized coil and the rotational uncooperative space target should be analyzed first. Here, the mechanisms of de-tumbling force are shown in Fig. 3.

The $\boldsymbol{B}$ induces eddy currents $\boldsymbol{J}$ within the rotating conducting target, which in turn interacts with $\boldsymbol{B}$ to produce a force $\boldsymbol{F_t}$ (i.e., de-tumbling force), as shown in Fig. 3(b). Meanwhile, the rotational speed $n_t$ of the target will be reduced under the action of $\boldsymbol{F_t}$, and the de-tumbling process can be realized.

Based on Lorentz force law, $\boldsymbol{F_t}$ acting on the rotating target can be obtained by integration over the target body $V$:

$$\boldsymbol{F_t} = \int_V \boldsymbol{J} \times \boldsymbol{B}\, dV \tag{1}$$

In addition, the target will also be subject to a de-tumbling torque $\boldsymbol{T}$:

$$\boldsymbol{T} = \int_V r \times \left( \boldsymbol{J} \times \boldsymbol{B} \right) dV \tag{2}$$

where $r$ is the radius of the target.

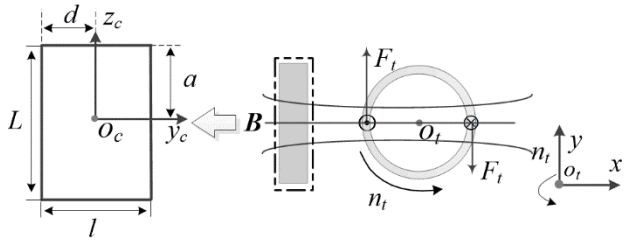


(a) (b)

Fig. 3. Structure parameters of the rectangular coil and the concept of de-tumbling force: (a) geometric structure parameters of the rectangular coil, and (b) de-tumbling force concept.

As shown in Figs. 3(a) and 3(b), the structure parameters of the Rectangular coil are: long side, $L$, wide side, $l$. The body coordinate system of the target, $O_t$ - $x_t y_t z_t$, and the fixed system of coil, $O_c$ - $x_c y_c z_c$.

To accurately calculate the magnetic field, the structure parameters of the coil are given as follows:

$$a = \frac{L}{2} \tag{3}$$

$$d = \frac{l}{2} \tag{4}$$

where $a$ is the length from $O_c$ to $l$, and $d$ is the length from $O_c$ to $L$.

### 2.1.3 *Modeling of Magnetic Field*

The de-tumbling robot carrying electromagnetic coil approaches the uncooperative space target through an orbit maneuver. $\boldsymbol{B}$ generated by an energized coil with current $\boldsymbol{I}$ will affect the magnitude of the $\boldsymbol{T}$ due to $T \propto B^2 \propto I^2$ [26-27], and $\boldsymbol{B}$ will vary with the change of the structure parameters of the coils when $\boldsymbol{I}$ is constant. However, the structure parameters of the coils cannot increase infinitely. Thus, there

must be optimal values that make the $\boldsymbol{B}$ is maximum. Apparently, it is necessary to analyze the relationship among them to find the optimal structure parameters.

It is interesting that when the angle between two coils is equal to 180° , it prevents the occurrence of non-zero $F_t$ and the attraction between the coils and the target caused by deviation and repulsion effects [12].

Concretely, the analytical model is established in Fig. 4. Among them, the excitation coils carried by the two de-tumbling robots are assumed to be $C_i\,(i=1,2)$. In addition, other parameters of $C_i\,(i=1,2)$ are represented by $i=1,2$, respectively.

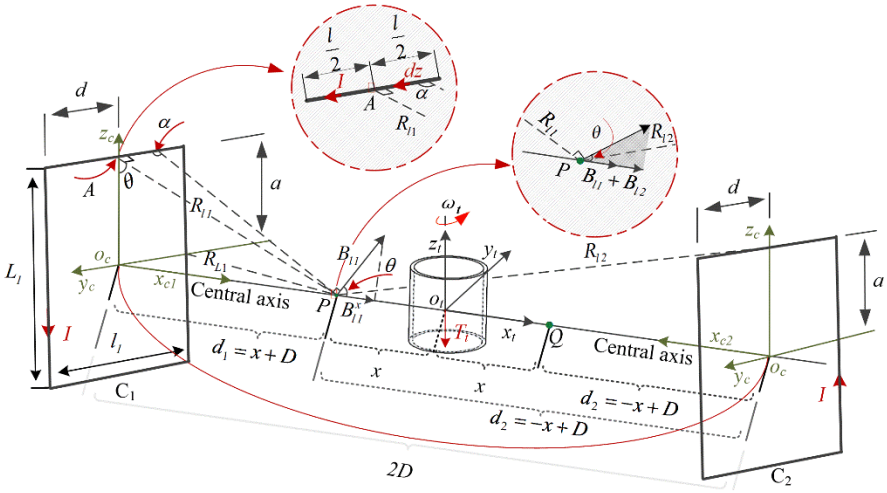


Fig. 4. Modeling of magnetic field analytical model.

The parameters in Fig. 4 are: the distance from $O_{ci}\,(i=1,2)$ to point $Q$, $d_i\,(i=1,2)$, the distance between $O_{c1}$ and $O_{c2}$, $2D$. The center of mass of the target lies on the $x_{ci}\,(i=1,2)$ axis of $C_i\,(i=1,2)$, $x_{ci}\,(i=1,2)$ axis is aligned with $x_t$ axis, and the distance from point $Q$ to $L_i, l_i\,(i=1,2)$ can be expressed as $R_{li}=\sqrt{\left[(d_i)^2+a^2\right]}$, and $R_{Li}=\sqrt{\left[(d_i)^2+d^2\right]}$, respectively, and the distance from $O_{ci}\,(i=1,2)$ to point $Q$ can be expressed as $d_1 = x + D$ and $d_2 = -x + D$, respectively.

Based on Biot-Savart law, the $\boldsymbol{B}$ generated by $C_i\,(i=1,2)$ carrying $\boldsymbol{I}$ can be expressed as follows [28]:

$$\boldsymbol{B}=\frac{\mu_0 N}{4\pi}\oint\frac{I d\boldsymbol{l}\times\boldsymbol{e_R}}{R^2}, \tag{5}$$

where $\mu_0 = 4\pi \times 10^{-7}\,(\mathrm{T \cdot m/A})$ is magnetic permeability of vacuum, $N$ represents the number of turns of coils, $Idl$ is an element of length along the coils, and $R$ and $\boldsymbol{e_R}$ are the distance and unit vector from source point to any field point in space, respectively.

The magnetic field model of the magnetic field $B_x$ along $x_{ci}\,(i = 1,2)$ axis of $C_i\,(i = 1,2)$ will be established in the following, as the axial component of $\boldsymbol{B}$ plays a crucial role in de-tumbling [27].

The magnetic field of point $Q$ can be obtained by addition of the vector field $\boldsymbol{B}$ on different sides of $C_i\,(i = 1,2)$. Firstly, the magnitude of $B_{li}\,(i = 1,2)$ generated by $l_i\,(i = 1,2)$ of $C_i\,(i = 1,2)$ at point $Q$ can be calculated as follows:

$$B_{li} = \frac{\mu_0 NI}{4\pi}\int_{-\frac{l}{2}}^{\frac{l}{2}} \frac{dy_{ci}}{y_{ci}^2 + R_{li}^2}\sin\alpha, \tag{6}$$

where $\sin\alpha = R_{li}\Big/\sqrt{y_{ci}^2 + R_{li}^2}$, and $\alpha$ is the inclined angle between $\boldsymbol{B_{li}}$ and $Idy_{ci}$. Then substituting $\sin\alpha$ into Eq. (6), $B_{li}\,(i = 1,2)$ can be obtained as follows:

$$B_{li} = \frac{\mu_0 NI}{2\pi R_{li}} \times \frac{l}{\sqrt{l^2 + 4R_{li}^2}}. \tag{7}$$

In addition, the inclined angle between central axis $O_{c1}Q$ or $QO_{c2}$ and the direction of $\boldsymbol{B_{li}}$ is $\theta_{li}\,(i = 1,2)$:

$$\theta_{li} = \arccos\left(\frac{a}{\sqrt{(d_i)^2 + a^2}}\right). \tag{8}$$

Next, the magnitude of $\boldsymbol{B_{li}}\,(i = 1\ or\ 2)$ lies on the central axis generated by $l_i\,(i = 1,2)$ of $C_i\,(i = 1,2)$ at point $Q$ can be calculated as follows:

$$B_{li,x} = B_{li}\cos\theta_{li}. \tag{9}$$

For convenience, similar to the above method, $B_{Li}\,(i = 1,2)$, and $\theta_{Li}$ can be obtained as

$$B_{Li} = \frac{\mu_0 NI}{2\pi R_{Li}} \times \frac{L}{\sqrt{L^2 + 4R_{Li}^2}}. \tag{10}$$

$$\theta_{Li} = \arccos\left(\frac{d}{\sqrt{\left(d_i\right)^2 + d^2}}\right). \tag{11}$$

For one coil (taking $C_1$ as an example to analysis), the magnitude of magnetic field generated by $C_1$ carrying $\boldsymbol{I}$ at any point in the x-axis direction can be calculated as follows:

$$B_x^{C_1} = 2\left(B_{li,x} + B_{Li,x}\right) \qquad i = 1. \tag{12}$$

For two coils, according to the symmetry, the magnitude of synthetic magnetic field generated by $C_i\ (i = 1,2)$ carrying $\boldsymbol{I}$ at any point in the x-axis direction can be calculated as follows:

$$B_x^{C_{1,2}} = \sum_{i=1}^{2}\left[2\left(B_{li,x} + B_{Li,x}\right)\right] \qquad i = 1,2. \tag{13}$$

## 2.2 Optimization Process

### 2.2.1 *Structure Parameters Analysis*

As analyzed above, the $\boldsymbol{B}$ generated by different coil structures after energizing is different. To enhance the de-tumbling performance, it is necessary to identify the structure parameters that result in the maximum $B_{max}$ on the target surface. At this moment, the corresponding coil parameters are the optimal. Here, for simplicity, the optimal parameters of one coil are analyzed first considering that the analysis process for two coils is similar. Concretely, by substituting the known parameters $R_{li}$, $R_{Li}$, $a$, and $d$ designed in "Initial Design and Theory Basis" Section into Eq. (12), respectively, then the magnetic field $B_x$ at $x_t$ can be obtained:

$$B_x = \frac{2\mu_0 NIL\,l\left(L^2 + 8d_1^2 + l^2\right)}{\pi\left(L^2 + 4d_1^2\right)\left(l^2 + 4d_1^2\right)\sqrt{L^2 + l^2 + 4d_1^2}}. \tag{14}$$

By observing Eq. (14), it can be concluded that the magnitude of $B_x$ is only related to the structure parameters $L$ and $l$ of the coils. Therefore, it is obvious that the problem of improving the de-tumbling performance is transformed into a parameters optimization. In addition, because the maximum size of the coils is determined by the diameter of the launcher fairing, the coil size in this model is restricted to be smaller than the maximum available radius of the current space launcher [29] (the diameter 4m of an Ariana 5 launcher) to fulfill the launch requirements. Thus, the nonlinear optimization model is built as follows:

*Objective function*:

$$max \quad B_x$$
$$Subject\ to: \qquad \sqrt{L^2+l^2} < D_{fairing}, \tag{15}$$

where $D_{fairing}$ is the diameter of the launcher.

More specifically, the fairing of launcher, the $D_{fairing}$, and the maximum coil structure parameters under constraints are shown in Fig. 5. Among them, $L$ = 3 m and $l$ = 2.5 m, respectively.

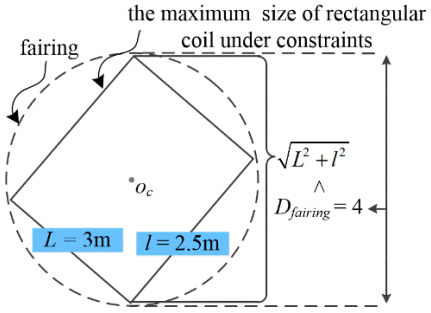


Fig. 5. The structure parameters of the fairing and Rectangular coil.

To find the coil structure parameters that maximize the magnetic field at different distances, Eq. (14) is written in mathematical software. Subsequently, optimal structure parameters are analyzed by traversing step length for $L$ and $l$. For convenience, the step length of 0.5 m is used for calculation, and the resulting data are presented in TABLE I. Throughout this process, the parameters listed in TABLE II are kept constant.

TABLE I
Optimal Rectangular coil Parameters at Different Distances

| **distance (m)** | **(*L*, *l*) or (*l*, *L*) (m)** | ***Bmax* (T)** |
|---|---|---|
| ⋮ | | ⋮ |
| $d$ = 10 | | $6.86\times10^{-6}$ |
| $d$ = 9 | | $9.33\times10^{-6}$ |
| ⋮ | (2.5, 3) | ⋮ |
| $d$ = 5 | | $4.93\times10^{-5}$ |
| ⋮ | | ⋮ |
| $d$ = 1 | (2.5, 2.5) | $1.14\times10^{-3}$ |
| $d$ = 0.8 | (2, 2) | $1.43\times10^{-3}$ |
| $d$ = 0.5 | (1.5, 1.5) | $2.24\times10^{-3}$ |
| $d$ = 0.3 | (1, 1) | $3.64\times10^{-3}$ |

TABLE II
Parameters Required for the Structure Parameters Model

| **Parameter** | **Describe** | **Value** |
|---|---|---|
| *I (A)* | Magnitude value of current | 50 |

It can be analyzed that due to the constraint, when $d$ > 1 m, the optimal coil structure parameters are always ($L$, $l$) = (2.5, 3) and remain unchanged. However, when $d$ < 1 m, the optimal coil structure parameters decreases with the decrease of $d$ and are no longer constrained. In addition, the $B_{max}$ increases with the decrease of $d$.

To further improve the de-tumbling performance, randomly choose $d$ = 1 m to analyze the electromagnetic properties, and the resulting data are presented in Fig. 6.

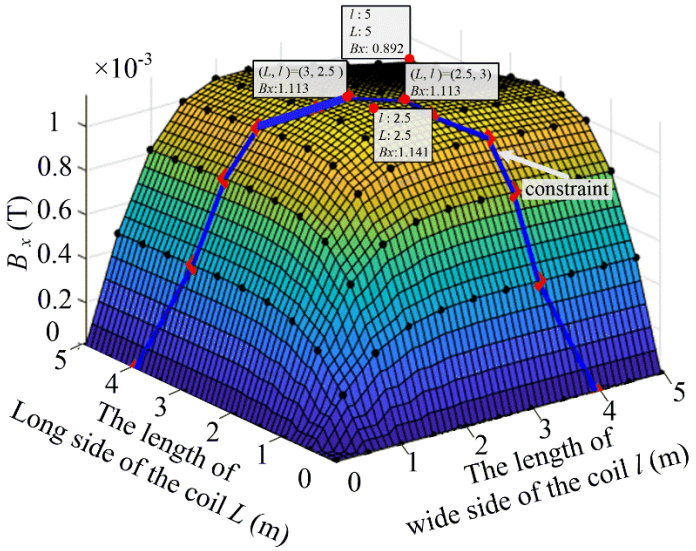


Fig. 6. The relationship between *Bx* and *L*, *l*.

Fig. 6 shows 3-D relationship between *Bx* versus *L* and *l*. According to the given relationship, it can be observed that in the constrained area indicated by the bold blue line (i.e., *L* < 4m, *l* < 4m), *Bx* increases rapidly with the increment of *L* and *l*. However, when (*L*, *l*) > (2.5, 2.5), *Bx* will decrease as *L* and *l* increases. It can be intuitively seen from the icons (*L*, *l*, *Bx*) = (5, 5, $0.892\times10^{-3}$) and (*L*, *l*, *Bx*) = (2.5, 2.5, $1.141\times10^{-3}$) that despite a 2 times increase in *L*, *Bx* has actually decreased. By comparing the (2.5, 2.5) icon with the icon of the maximum size of the coil under constraint, i.e., (2.5, 3), the same phenomenon can also be concluded. Hence, the larger *L* and *l* do not imply the larger *Bx*. So, it can be concluded that the optimal structure parameters of the rectangular coil are (*L*, *l*) = (2.5, 2.5). At these parameters, the magnetic field *Bx* at the target is maximum, and it satisfies the constraint $\sqrt{L^2+l^2}=\sqrt{2.5^2+2.5^2}<D_{fairing}$.

### 2.2.2. *Influence of Current Direction for Coils on Magnetic Field*

To enhance the de-tumbling performance, besides determining the optimal structural parameters, it is also to assess the influence of current direction in $C_i$ ($i$ =1, 2) on de-tumbling efficiency, as shown in Fig. 7.

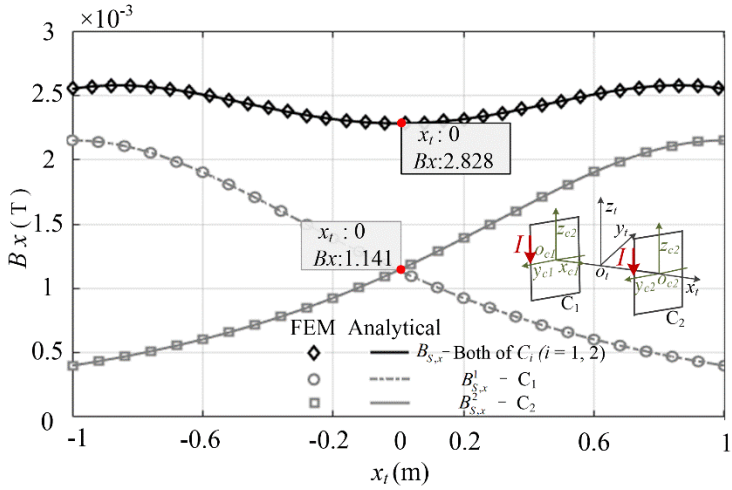


a) I in the same direction for Ci (i =1, 2)

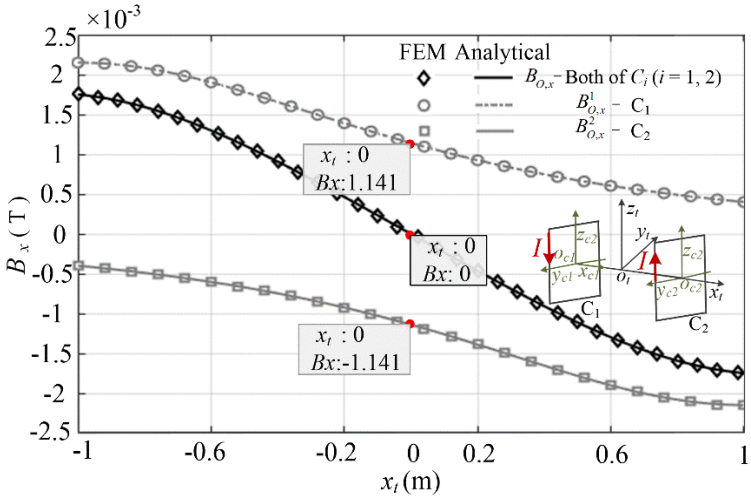


b) I in the opposite direction for Ci (i =1, 2)

Fig. 7. Different current direction for energized Ci (i =1, 2).

The magnetic fields generated by $C_1$, $C_2$, or both of $C_i$ ($i$ =1, 2) are all investigated through analytical model of magnetic field and FEM when $\boldsymbol{I}$ for $C_i$ ($i$ =1, 2) flows in the same or opposite direction, as shown in Figs. 7(a) and 7(b), respectively. This analysis helps to understand the characteristics of the magnetic field when the current passes through $C_i$ ($i$ =1, 2) in two different directions as described above, providing the de-tumbling task. Additionally, Fig. 7 demonstrates that the results obtained from the proposed analytical model of magnetic field and FEM are in good agreement, further confirming the accuracy of both methods.

More specifically, it can be seen from Fig. 7(a) that magnetic field $B_{S,x}^1$ and $B_{S,x}^2$ at $O_{ci}\left(i=1,2\right)$ of $C_1$ and $C_2$ are the maximum, and then gradually decreases as the

distance from $O_{ci}\ (i=1,2)$ increases. Further, the total magnetic field $B_{S,x}$ along $x_{ci}\ (i=1,2)$ axis of $C_i\ (i=1,2)$ is the sum of $B_{S,x}^1$ and $B_{S,x}^2$, and the smaller the $|x_t|$, the smaller the $B_{S,x}$. However, it can be seen from Fig. 7(b) that the magnetic field $B_{O,x}^1$ generated by $C_1$ is equal to $B_{S,x}^1$, whereas the magnetic field $B_{O,x}^2$ generated by $C_2$ is equal to $-B_{S,x}^2$, resulting in a total magnetic field $B_{O,x}$ smaller than $B_{S,x}$. It can be concluded that the occurrence of this different characteristic is caused by the opposite direction of $\boldsymbol{I}$ for $C_i\ (i=1,2)$.

Therefore, based on the above analysis, the optimal model to de-tumble the target is to have $\boldsymbol{I}$ for $C_i\ (i=1,2)$ flowing in the same direction, producing the maximum magnetic field, as shown in Fig. 7(a). In addition, the values of $B_{S,x}^1$, $B_{S,x}^2$, $B_{O,x}^1$ or $B_{O,x}^2$ at the center of mass of the target (i.e., $x_t = 0$ ) are equal to $1.141\times10^{-3}$ T, which matches the values for ($L$, $l$) = (2.5, 2.5) shown in Fig. 6, further confirming the accuracy of the established model.

## 2.3 Analysis of Optimization Results

The optimal structure parameters of the coil are determined in “Optimization Process” Section based on the magnetic field analytical model established in “Initial Design and Theory Basis” Section. Subsequently, this section applies the optimal parameters to $C_i$ ($i$ =1, 2). Several different numerical simulations based on FEM are then conducted for a hollow cylindrical uncooperative space target to further analyze and draw guiding conclusions.

### 2.3.1 *Improved De-tumbling Torque Method*

As shown in Fig. 7(a), $B_{S,x}$ generated by the designed rectangular energized coil has a spatial gradient due to the different magnitude of $B_{S,x}$ at different $x_t$. Consequently, the de-tumbling torque cannot be calculated using a de-tumbling torque model based on the assumption of a uniform magnetic field [14], [30]. Therefore, to calculate the de-tumbling torque of the uncooperative space target, Maxwell's stress tensor method can be employed as follows [31]:

$$F_\theta = \frac{L_t r_{air}}{\mu_0}\int_0^{2\pi} B_r B_\theta d\theta \tag{16}$$

$$T = \frac{L_t r_{air}^2}{\mu_0}\int_0^{2\pi} B_r B_\theta d\theta, \tag{17}$$

where $B_r$ and $B_\theta$ are the radial and tangential components of the magnetic field at $r_{air}$, respectively, and $L_t$ is the axial length of the target. Among them, $r_{air}$ is the radius of the cylinder that encloses the target.

To calculate the de-tumbling torque of Eq. (17), a transformation is applied to convert the magnetic field in Cartesian coordinate system to the magnetic field in Cylindrical coordinate system. $B_r$ and $B_\theta$ are defined as:

$$\begin{cases} B_r = B_x\cos\theta + B_y\sin\theta \\ B_\theta = -B_x\sin\theta + B_y\cos\theta \end{cases}, \tag{18}$$

where $B_x$ and $B_y$ are the normal and tangential components of the magnetic field in Cartesian coordinate system, respectively.

The detailed structure parameters of the target for numerical simulations are listed in TABLE III, and the magnetic field at $r_{air}$ is given first by FEM, which is shown in Fig. 8.

TABLE III
The Structure Parameters of the Target

| Parameter | Describe | Value |
|---|---|---|
| $b_g$ (mm) | Thickness of the target | 10 |
| $\sigma$ (S/m) | Conductivity of the target | $3.8\times10^7$ |
| r (m) | Radius of the target | 0.1 |
| $Lt$ (m) | Axial length of the target | 2r |
| $\omega$ (rad/s) | Angular velocity of the target | $\pi$ |

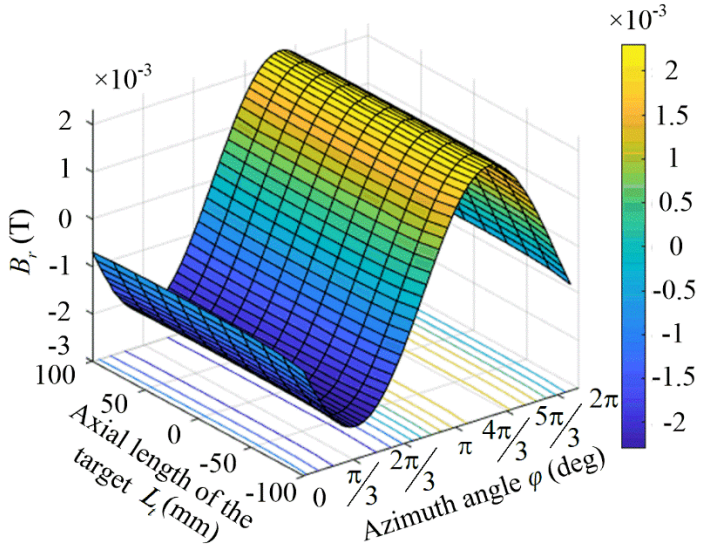


a) Radial components of the magnetic field.

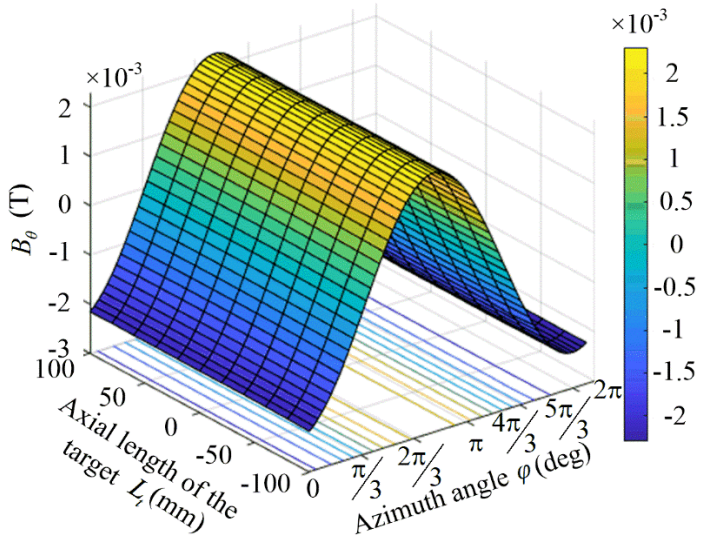


b) Tangential components of the magnetic field.

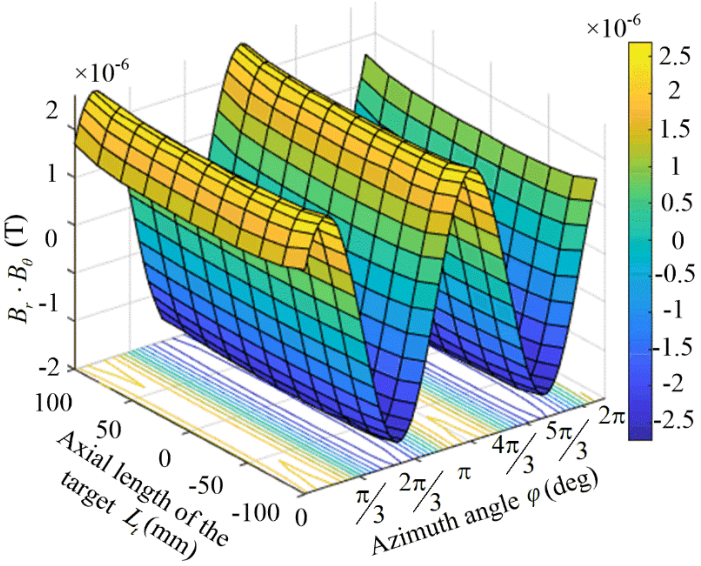


c) The product of both components of the magnetic field

Fig. 8. Magnetic field at $r_{air}$ when $r$=0.1 m.

$B_r$, $B_\theta$ and $B_r \cdot B_\theta$ at $r_{air}$ are calculated by FEM shown in Fig. 8(a), Fig. 8(b) and Fig. 8(c), respectively. It can be noted that $B_r$ and $B_\theta$ exhibit regular changes with $\varphi \in [0,2\pi]$. This is due to the designed coil structure, together with the shape of the target, jointly determines this phenomenon. Then, it can also be noted from Fig. 8(c) that the magnitude of $B_r \cdot B_\theta$ along the axial direction [i.e., $L_t$] is different. As it moves away from the center of mass of the target $O_t$, its value increases.

According to the physical mechanism deduced by Maxwell's stress tensor method, Eq. (17)is suitable for the model (e.g., the coils are placed in a stator made of silicon steel sheet) with constant axial magnetic field. However, due to the magnitude of $B_r \cdot B_\theta$ along the axial direction of the target is different in the model of this study, which causes Eq. (17)to be no longer applicable.

For high accuracy, an improved method is proposed. The rotor's axial length is discretized into segments, as shown in Fig. 9(a), and subsequently, the de-tumbling torque for each segment length is computed. The de-tumbling torque from all segments are then summed up. Notably, as the number of segments increases, the computed de-tumbling torque value approaches the true value more closely under the limit of summation.

The improved de-tumbling torque calculation method can be obtained as follows:

$$T = \sum_{n=1,2,3L N_{seg}}^{n=N_{seg}} \frac{L_t r_{air}^2}{\mu_0 N_{seg}} \int_0^{2\pi} B_{r,n}\left(\frac{L_t}{N_{seg}}\right) B_{\theta,n}\left(\frac{L_t}{N_{seg}}\right) d\theta, \tag{19}$$

where $N_{seg}$ is the number of segments along the axis of the target, $n$ represents index of the segments, and $B_{r,n}\left(\frac{L_t}{N_{seg}}\right)$ and $B_{\theta,n}\left(\frac{L_t}{N_{seg}}\right)$ represent radial and tangential components of the magnetic field at different indices, respectively.

In addition, for clarity, $r_{air}$ in Eq. (17)and Eq. (19), and other structure parameters of the target are further shown in Figs. 9(b) and 9(c).

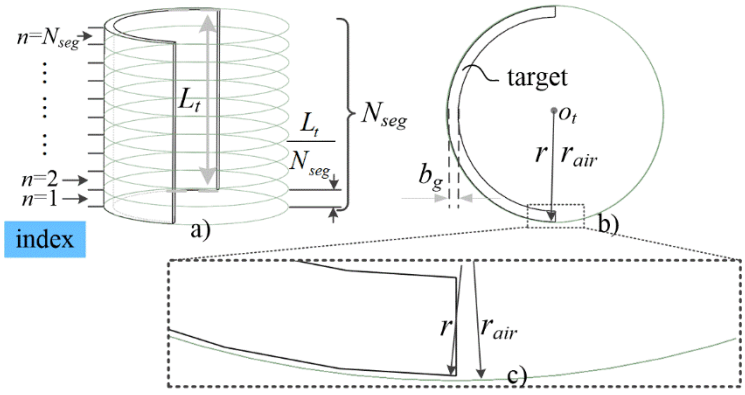


Fig.9. Schematic diagram of axial segmentation and structure parameters of the target.

### 2.3.2 *De-tumbling Torque Characteristics*

By substituting $B_r \cdot B_\theta$ calculated by FEM shown in Fig. 8(c) into Eq.(19), the de-tumbling torque acting on the target can be obtained, which is a key step to solve the de-tumbling problem. Among them, the de-tumbling torque of different numbers of

segments when $r$=0.1 m is analyzed through FEM computations, as shown in Fig. 10. When the target radius varies from 0.1 m to 0.8 m with a step size of 0.1 (i.e., $r \in [0.1:0.1:0.8]$), the resulting de-tumbling torque is shown in Fig. 11.

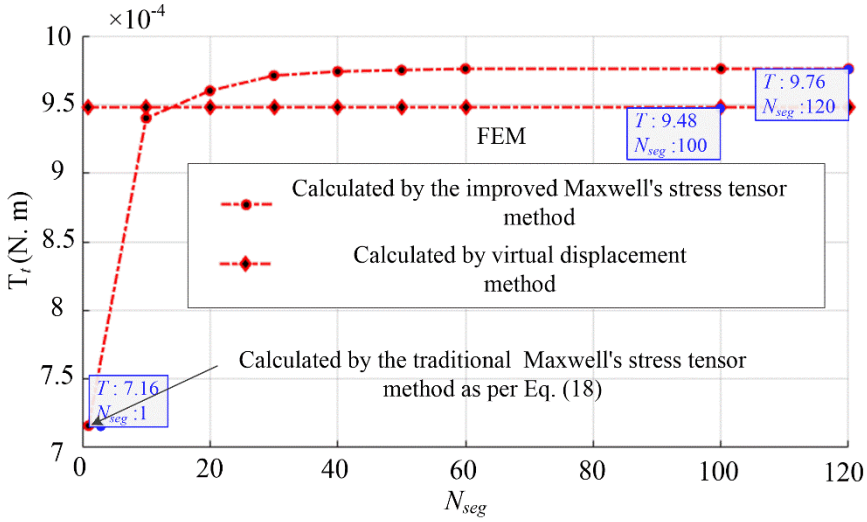


Fig. 10. De-tumbling torque of different numbers of segments when r=0.1 m, Nseg.

It can be seen that de-tumbling torque increases with the increase of $N_{seg}$, and as $N_{seg}$ reaches 40, the computed de-tumbling torque converges more closely to the true value under the summation limit. Furthermore, compared to the de-tumbling torque calculated using the traditional Maxwell's tensor method, i.e., Eq. (17)with $N_{seg}$ = 1, as shown in Fig. 10, the accuracy of the de-tumbling torque calculated using the proposed improved Maxwell's stress tensor method in this paper has been improved by 26.64 %. This improvement also validates the advantage of the proposed method. In addition, the accuracy of the Maxwell's stress tensor method is further verified by comparing the de-tumbling torque of the improved Maxwell's stress tensor method with that of the virtual displacement method [32]. The error decreases gradually with an increasing number of the segments, and when $N_{seg}$ > 40, the minimum error is only 2.87%.

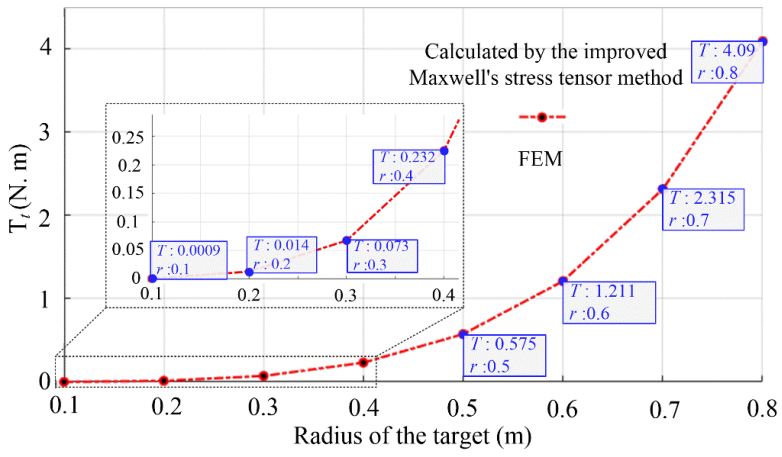

Fig. 11. De-tumbling torque of targets with different radii.

Fig. 11 illustrates the variations in the de-tumbling torque by the target at different target radii. It can be observed that as the target radius increases, the de-tumbling torque exerting on the target also increases, which matches the relationship between the de-tumbling torque and radius shown in Eq. (19).

## 3. Results and conclusion

An optimization framework is proposed in this article for the optimal coil structure for braking the uncooperative space targets, which has focused on coil's structure parameters analysis, magnetic field analytical modeling, and electromagnetic characteristics analysis. Firstly, the optimal structure parameters for different distances between the coils and the target are studied, when the magnetic field at the target is maximum. Then, the electromagnetic characteristics of two coils with different current directions are conducted. The effectiveness of the proposed magnetic field analytical model is verified using FEM, and the results show good agreement. The results indicate that when the distance is less than 1m, the constraint size of the transmitter fairing is no longer limited, and the magnetic field generated at the target is maximum when the direction of current flow in both coils is the same. Additionally, the accuracy of the de-tumbling torque is improved 26.64 % when calculated using the improved Maxwell's stress tensor method compared to the traditional Maxwell's stress tensor method. The accuracy is verified by the virtual displacement method and the traditional Maxwell's stress tensor method.

### Author Contributions

L. Du conceived the idea and wrote the original draft. L. Du, Z. Chen and H. Hu jointly developed the problem. X. Liu and Y. Guo helped to revise the manuscript. All authors have read and agreed to the published version of the manuscript.


### Acknowledgment

This work was supported by the National Natural Science Foundation of China (11972078).


### Conflicts of Interest

The authors declare that there is no conflict of interest.

### Data Availability

All relevant data are within the paper.

## Reference


[1] Kuznetsov VD, Sinelnikov VM, Alpert SN. Yakov Alpert: Sputnik-1 and the first satellite ionospheric experiment. *Adv. in Sp. Res.* 2015; 55(12): 2833-2839.

[2] Liou JC, Johnson NL. Instability of the present LEO satellite populations. *Adv. in Sp. Res.* 2008; 41(7): 1046-1053.

[3] Kessler DJ, Courpalais BG. Collision frequency of artificial satellites: The creation of a debris belt. *J. Geophys Res-Space.* 1978; 83(A6): 2637-2646.

[4] Shan M, Guo J, Gill E. Review and comparison of active space debris capturing and removal methods. *Prog. Aerosp. Sci.* 2016; 80(12): 18–32.

[5] Yoshida K. Achievements in space robotics. *IEEE Robot & Autom. Magazine*. 2009; 16(4): 20-28.

[6] Nishida SI, Kawamoto S. Strategy for capturing of a tumbling space debris. *ACTA Astronaut.* 2011; 68(1-2): 113-120.

[7] Papushev P, Karavaev Y, Mishina M. Investigations of the evolution of optical characteristics and dynamics of proper rotation of uncontrolled geostationary artificial satellites. *Adv. in Sp. Res.* 2009; 43(9): 1416-1422.

[8] Huang PF, Cai J, Meng ZJ, Hu ZH, Wang DK. Novel method of monocular real-time feature point tracking for tethered space robots. *J. Aerosp. Eng.* 2014; 27(6).

[9] Reed J, Barraclough S. Development of harpoon system for capturing space debris. in Proc. 6th European Conference on Space Debris, Darmstadt, Germany, in: ESA Special Publication,2013.

[10] Sugai F, Abiko S, Tsujita T, Jiang X, Uchiyama M. Detumbling an uncontrolled satellite with contactless force by using an eddy current brake. in *Proc. IEEE/RSJ International Conference on Intelligent Robots and Systems*. 2013; 783-788.

[11] Sugai F, Abiko S, Tsujita T, Jiang X, Uchiyama M. "Development of an eddy current brake system for detumbling malfunctioning satellites," in *Proc. IEEE/SICE International Symposium on System Integration (SII)*, 2012; 325-330.

[12] Du L, Chen Z, Hu HZ, Zhao J, Liu XD, Zhang Q, Zhang KM. Contactless de-tumbling of the uncooperative targets using arc-linear electro-magnetic device. *Adv. in Sp. Res.* 2023; 71(8): 3290-3300.

[13] Liu X G, Lu Y, Zhang Q, Zhang KM. An application of eddy current effect on the active detumble of uncontrolled satellite with tilt air gap. *IEEE Trans. Magn.* 2019; 55(12): 1-11.

[14] Li M, Zhang Y, Zhang JR, Lin HY, Yang FR. Detumbling method for uncontrolled satellite based on eddy currents. *J. Guid. Control Dyn.* 2020; 43(8): 1444-1455.

[15] Meng QL, Zhao C.Z, Ji HX, Liang JX. Identify the full inertial parameters of a non-cooperative target with eddy current detumbling. *Adv. in Sp. Res.* 2020; 66(7): 1792-1802.

[16] Gomez NO, Walker SJI. Guidance, navigation, and control for the eddy brake method. *J. Guid. Control Dyn.* 2017; 40(1): 52-68.

[17] Gomez NO, Walker SJI. Eddy currents applied to de-tumbling of space debris: Analysis and validation of approximate proposed methods. *Acta Astronaut.* 2015; 114, 34-53.

[18] Yu YF, Yang F, Yue HH, Lu YF, Li SZ, Zhao HH. Prospects of de-tumbling large space debris using a two-satellite electromagnetic formation. *Adv. in Sp. Res.* 2021; 67(6): 1816-1829.
[19] Wan WY, Sun C, Zheng ZX, Yuan JP. Non-cooperative space target de-tumbling approach using multiple high-temperature superconducting coils. *J. Guid. Control Dyn.* 2022; 45(7): 1229-1240.
[20] Yu YF, Yue HH, Zhao HH, Yang F, Chen X. Optimal configuration of distributed HTS coils for the non-contact de-tumbling of space debris. *ACTA Astronaut.* 2022; 191, 491-501.
[21] Bennett T, Schaub H. Contactless electrostatic detumbling of axi-symmetric GEO objects with nominal pushing or pulling. *Adv. in Sp. Res.* 2018; 62(11): 2977-2987.
[22] Peters TV, Escorial Olmos D. COBRA contactless detumbling. *CEAS Space Journal*. 2016; 8(3): 143-165.
[23] Vetrisano M, Thiry N, Vasile M. Detumbling large space debris via laser ablation. in *Proc. IEEE Aerospace Conf.*, Big Sky, MT, USA, 2015; 1-10.
[24] Kadaba PK, Naishadham K. Feasibility of noncontacting electromagnetic despinning of a satellite by inducing eddy currents in its skin I. Analytical considerations. *IEEE Trans. Magn.* 1995; 31(4): 2471-2477.
[25] Vinti JP. Theory of the spin of a conducting space object in the magnetic field of the Earth. *Ball. Res. Lab.*, *Rep.* 1957.
[26] Boyle JC, Greyerbiehl JM, Mosher EJ. Experimental determination of eddy current torques on bodies rotating relative to a uniform magnetic field. NASA Technical Note D-5086, United states: 1969.
[27] Shi YK, Yang LP, Zhu YW, and Chu FD. Modeling and simulation of superconducting eddy brake concept for space tumbling object. *J. Astronaut.* 2018; 39(10): 1089-1096.
[28] Jackson JD. Classical Electrodynamics, 3rd ed. New York, NY, USA: Wiley, 1998.
[29] Arianespace S.A., Ariane 5 User's Manual, Issue 5, Revision 1, July 2011.
[30] Youngquist RC, Nurge MA, Starr SO, Leve FA, Peck M. A slowly rotating hollow sphere in a magnetic field: First steps to de-spin a space object. *Am. J. Phys.* 2016; 84:181–191.
[31] Zarko D, Ban D, Lipo TA. Analytical solution for electromagnetic torque in surface permanent-magnet motors using conformal mapping. *IEEE Trans. Magn.* 2009; 45(7): 2943-2954.
[32] Liu JQ, Bai JG, Zheng P, Zhang SK, Yin ZS. Torque Analysis of Magnetic-Field-Modulated Double-Rotor Machines with Virtual Work Method. *21st International Conference on Electrical Machines and Systems (ICEMS)*. 2018.